

Full length article

A synchrotron X-radiography study of the fragmentation and refinement of primary intermetallic particles in an Al-35 Cu alloy induced by ultrasonic melt processing



Feng Wang^{a,*}, Dmitry Eskin^a, Jiawei Mi^b, Chuangnan Wang^b, Billy Koe^b, Andrew King^c, Christina Reinhard^d, Thomas Connolley^d

^a Brunel Centre for Advanced Solidification Technology (BCAST), Brunel University London, Uxbridge, UB8 3PH, UK

^b School of Engineering & Computer Science, University of Hull, Hull, East Yorkshire, HU6 7RX, UK

^c Synchrotron SOLEIL, L'Orme des Merisiers, Saint-Aubin, BP 48 91192, Gif-sur-Yvette Cedex, France

^d Diamond Light Source Ltd, Harwell Science & Innovation Campus, Didcot, OX11 0DE, UK

ARTICLE INFO

Article history:

Received 7 June 2017

Received in revised form

4 September 2017

Accepted 7 September 2017

Available online 9 September 2017

Keywords:

Solidification

Fragmentation

Synchrotron X-ray radiography

Ultrasonic melt processing

Intermetallic refinement

Abstract

Using synchrotron X-ray high speed radiography, the fragmentation and refinement of pre-existing primary Al₂Cu intermetallic dendrites induced by ultrasonic melt processing in a hypereutectic Al-35% Cu alloy were studied in-situ and in real time. The alloy was melted, contained and processed in a quartz tube crucible with a middle section of approximately 300 μm-thick channel where the observations were made. Direct observation of intermetallic fragmentation and detachment unambiguously confirms that the acoustic cavitation and streaming flow play a crucial role in fragmentation of the intermetallic dendrites. Furthermore, the remelting effect due to transport of hot liquid via acoustic streaming flow and the stress against the intermetallic dendrites caused by acoustic streaming flow are found to be the dominant fragmentation mechanism in the present experiments. It is also suggested that cavitation bubbles or bubble clouds contribute to fragmentation not only by mechanically fracturing the dendrites but also by facilitating the effect of acoustic streaming flow on dendrites. At last, clear observation of equiaxed intermetallic dendrites growing from small fragments after ultrasonic melt processing provides the first conclusive evidence of the refinement mechanism, i.e. the acoustic cavitation and acoustic streaming flow progressively break the intermetallic dendrites into small fragments. Most of these small fragments are able to survive and then act as nuclei for the subsequent solidification of intermetallic phases, consequently leading to intermetallic refinement in the solidified microstructure.

© 2017 Acta Materialia Inc. Published by Elsevier Ltd. This is an open access article under the CC BY license (<http://creativecommons.org/licenses/by/4.0/>).

1. Introduction

Application of high-intensity ultrasonic vibrations to processing of liquid or semi-solid metals and their alloys during solidification has attracted considerable interest from the research community and casting industry. Ultrasonic melt processing (USMP) induces significant beneficial microstructural changes, for example, the refinement of matrix grains and primary particles, the improvement of structural and chemical homogeneity and the decrease of porosity [1–3]. USMP is also a promising technology that can offer a sustainable, energy-efficient and pollution-free solution for the industry to manufacture many different conventional and

advanced metals and alloys [1–3]. However, the application of USMP in real industrial practice has been very limited. One of the reasons behind this is the lack of in-depth understanding of the precise mechanisms that are responsible for various USMP-induced benefits.

It is recognised that the influence of USMP on microstructure arises from two important phenomena: (i) acoustic cavitation which refers to the formation, growth and implosive collapse of cavitation bubbles and (ii) acoustic streaming that is the formation of a quasi-steady state flow driven by acoustic wave propagation and cavitation zone pulsation [3–6]. Based on these phenomena, a variety of mechanisms have been proposed to elucidate the USMP-induced refinement effect. In general, they can be classified into two theories: (1) the cavitation-enhanced nucleation theory and (2) the cavitation-induced fragmentation theory [1,3,4]. The

* Corresponding author.

E-mail address: feng.wang@brunel.ac.uk (F. Wang).

cavitation-enhanced nucleation theory further consists of two mechanisms. One is based on the local increase of melt undercooling resulting from an increase of the melting point caused by the instantaneous pressure spike immediately after the collapse of cavitation bubbles. This mechanism was demonstrated as early as in the 1960s by Hunt and Jackson [7] who carried out experiments on benzene and water, and by Frawley and Childs [8] who used bismuth and Bi-Sn alloys. Nevertheless, the survival of the newly-formed solid crystals in the melt, especially when the USMP is applied above the liquidus temperature, is still under debate. The other cavitation-enhanced nucleation mechanism [3,5] suggests that the formation, growth and implosive collapse of cavitation bubbles produces a high-energy shockwave or liquid jet flow near impurity particles. Both would improve wetting of the impurity particles by the melt and hence activate them to become effective nucleation sites for solid phase formation. Recent investigation [9] by the authors on the refinement of primary Al₃Ti intermetallic particles induced by USMP in a completely liquid Al-0.4 wt% Ti alloy revealed that the cavitation-enhanced heterogeneous nucleation of primary Al₃Ti intermetallic on α -Al₂O₃ particles is the primary mechanism contributing to the observed refinement, which strongly supports the mechanism based on the activation of impurity particles by cavitation bubbles. The cavitation-induced fragmentation theory [1,4,6,10] postulates that the impact generated by bubble pulsation and/or implosion on the solid crystals already formed in the melt is strong enough to fragment them. The solid fragments are then distributed throughout the melt via the acoustic streaming, becoming perfect nuclei for subsequent solidification and eventually multiplying the number of solid crystals, leading to refinement. Again, the survival of the solid fragments when transferred to the bulk melt is also an issue of dispute. Although a vast amount of results obtained from numerous dedicated solidification experiments followed by advanced characterisation [9,11–13] have made progress in understanding the mechanisms underlying the beneficial effects of USMP, almost all of these results are based on post-solidified microstructure analyses and hence are essentially indirect evidence. In addition, these results reveal little direct information on the dynamic aspects of solidification under the effect of USMP.

Direct observation of the solidification process in the presence of USMP is therefore of great importance to deepen our understanding. A number of investigations [14–18] have been carried out to study the effect of ultrasound on solidification process in-situ and in real time using transparent analogue alloys. The results have been useful in verifying the proposed cavitation-enhanced nucleation and cavitation-induced fragmentation theories. However, it is increasingly realised that the distinct difference in the physical and mechanical properties between real metallic alloys and transparent analogue alloys may affect the exact mechanisms underlying the USMP-induced effects. In addition, few observations have been made with sufficient temporal and spatial resolution, due to the highly dynamic behaviour of cavitation bubbles and their interactions with solid crystals, and the limitation of experimental apparatus, particularly the imaging speed of the cameras. As a consequence, the in-situ observation of the solidification of real metallic alloys under the effect of USMP with sufficient spatio-temporal resolution is highly desirable, but very difficult to achieve. In the past decade or so, with the rapid development in synchrotron radiation sources and in high-speed digital cameras, in-situ synchrotron X-ray imaging (radiography and tomography) has emerged as a powerful tool for studying many aspects of solidification processes [19–27]. Among published studies, a few attempts [28–34] have been made to study the solidification of metallic

alloys under the effect of USMP. Mi's group [28–30] was among the first to use the ultrafast synchrotron X-ray imaging to study the shockwaves and enhanced flows in Sn-13% Bi and Bi-8% Zn alloys. Later, Huang et al. [32], Xu et al. [33] and Mirihanage et al. [34] used synchrotron X-ray radiography to measure the size distribution, average radius, growth rate and number density of cavitation bubbles in an Al-10 wt% Cu alloy respectively. In addition, Tzanakis et al. [31] observed instantaneous re-filling of a micro-capillary channel with melt in an Al-10% Cu alloy which provides the direct evidence for the ultrasonic capillary effect. However, there is still lack of systematic studies of real-time observations to provide conclusive validation of the mechanisms proposed for USMP-induced microstructural refinement.

In our work present in this paper, we have used high speed synchrotron X-ray radiography to study the solidification of primary Al₂Cu intermetallic phase under the effect of USMP and to capture the dynamic interaction between cavitation bubbles and primary Al₂Cu intermetallic particles in situ and in real time. We believe that the results provide direct evidence to clarify and gain fresh insight into the mechanisms that govern the primary intermetallic fragmentation and refinement induced by USMP.

2. Experimental

In situ high speed synchrotron X-ray radiography experiments were conducted at the Pression Structure Imagerie par Contraste à Haute Énergie (PSICHÉ) beamline of Synchrotron SOLEIL, France [35] using the dedicated in-situ ultrasound solidification apparatus designed by Mi et al. [29,30].

The experimental setup at the beamline is shown in Fig. 1. It comprises three major parts: (1) a furnace with a crucible part for melting and solidification, Fig. 1 (a & b); (2) an ultrasonic processing part, Fig. 1 (c); and (3) a high-speed imaging part, Fig. 1(d).

The melting and solidification of the alloy samples was carried out in the custom-made quartz tube crucible inside a two-zone furnace. The quartz tube has a 10 mm inner diameter with a flattened thin channel in the middle of ~300 μ m thickness. A picture of the quartz tube and a schematic of the cross section of the central thin channel are shown in the insets of Fig. 1(e). This special crucible was made to facilitate the introduction of ultrasound wave and the X-ray transmission. The two-zone furnace consists of top and bottom halves with independent thermal control.

The ultrasonic melt processing was implemented with a niobium sonotrode driven by a Hielscher UP100H ultrasonic piezoelectric, air cooled transducer. The ultrasound transducer had a fixed frequency of 30 kHz and adjustable input power of 0–100 W with a maximum acoustic power density of 600 W/cm². Niobium sonotrodes 58 mm long with a tip diameter of 1 mm were used and positioned in the melt at the wedge area above the thin channel to transmit ultrasonic waves into the melt inside the thin channel. The whole ultrasound unit was mounted on a linear motorized stage so that it could be lowered into the melt and lifted back up to original position after USMP was stopped.

The radiography videos were recorded by a Vision Research Miro 310 M high speed CMOS camera, attached to the X-ray imaging optics (5 \times magnification) of the Psiché beamline. Contrast in the radiographs of the alloy samples was optimised by modifying the incident beam spectrum, using mirror optics to reject high energy photons and filtration to remove low energy photons. For the Al-35%Cu alloy, optimum imaging conditions were obtained for an X-ray mirror angle of 2.5 mrad, combined with 5 μ m Al and 300 μ m Cu filters, giving a “filtered pink beam” with an average detected energy of 34 keV. The source characteristics and imaging

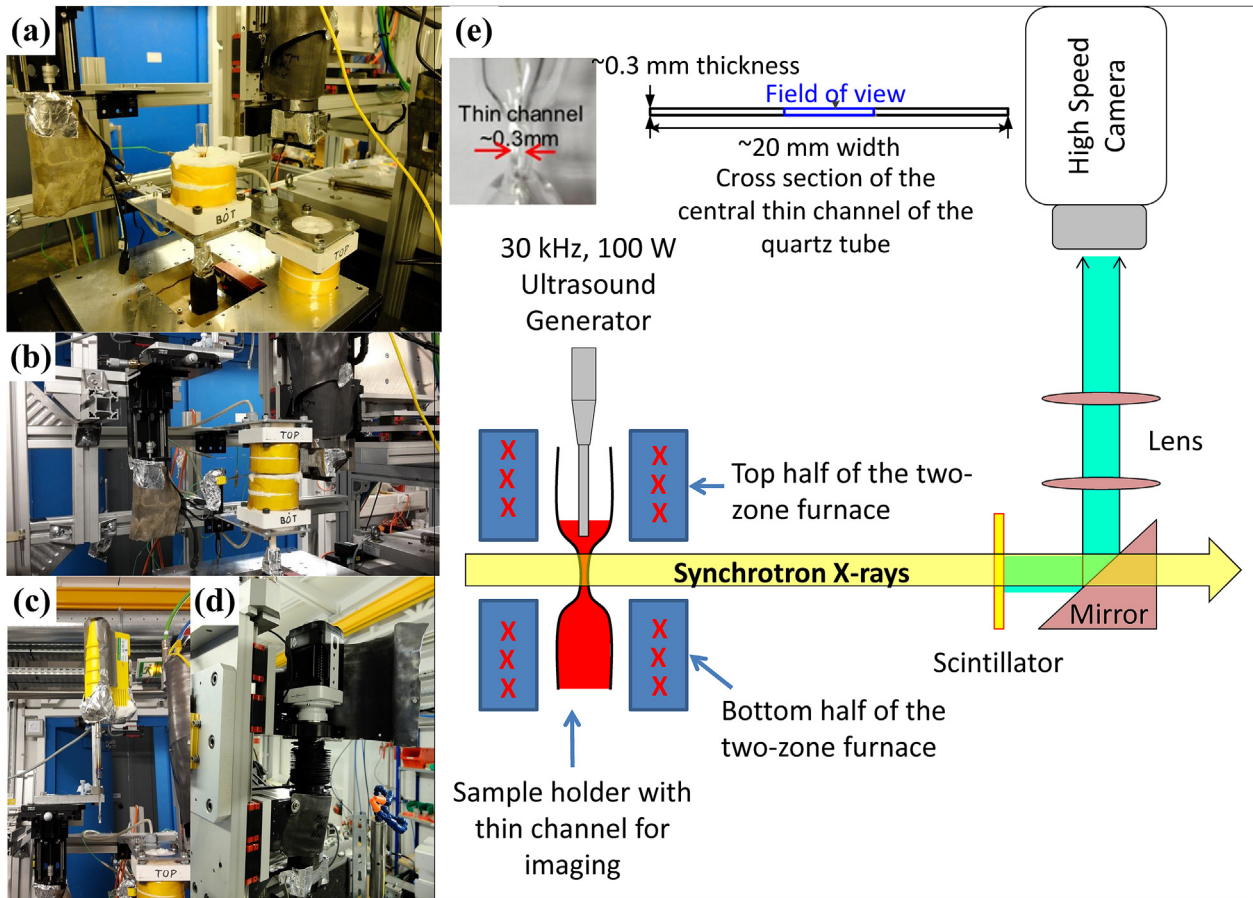


Fig. 1. Experimental setup at the PSICHÉ beamline of SOLEIL: (a) the position of a custom-made quartz tube in a two-zone furnace; (b) the two-zone furnace for melting the alloy; (c) ultrasound generator with sonotrode; (d) high speed camera; and (e) a schematic of the experimental setup. Adapted from Fig. 1 of Ref. [29].

setup enabled fast radiography at 1000 frames per second (fps) during the application of USMP to samples, followed by slower image recording at 1 or 4 fps during controlled cooling of the samples. With high speed imaging, the choice of parameters is often a compromise between frame rate, exposure, available field of view and total recording time. The Miro 310 M camera, like other standard high speed cameras, achieves high frame rates by capturing images into on-board RAM (12 GB capacity). Recording speed is partly determined by the data transfer rate from the sensor to RAM. Higher speeds can be achieved by reducing the region of interest captured by the sensor. However, this reduces the available field of view, and higher recording speeds also require shorter exposure times, which may result in under-exposure. Finally, higher frame rates, and hence data rates, reduce the available recording time before the camera's RAM is filled. In our case, we wanted to capture a wide field of view, so used 1280×656 pixels of the camera sensor. This translates to a field of view of $5120 \times 2624 \mu\text{m}^2$ at $4 \mu\text{m}/\text{pixel}$. Dual speed recording was achieved by partitioning the camera's RAM into two. Partition 1 was used during USMP at 1000 fps, giving a recording time of 5 s. Partition 2 was used for recording during slow cooling after USMP. The same exposure time was used, and by gating the camera's acquisition, the recording speed and hence total recording time could be selected. Slow cooling was recorded at 1 or 4 fps, giving a recording time of 84 min at 1 fps or 21 min at 4 fps. At 1000 fps, the longest possible exposure time was 0.996 ms, which gave adequate exposure in the images.

The top of the field of view for imaging was 2 mm below the sonotrode. It was considered that setting the field of view closer to the sonotrode tip was unfeasible at 1000 fps. Near the sonotrode, which operates at 30 kHz, the cavitation zone was highly dynamic, with a high number density of bubbles generated. Imaging here without motion blur would have required much higher frame rates (at least 60 kHz) as demonstrated in a related study reported in Ref. [36] and hence unfeasibly short exposure times, given the available X-ray source characteristics. Imaging of bubble dynamics at higher speeds at synchrotron light sources is possible, for example at beamline 32-ID of the APS, as described in previous work [29,30].

The detailed experimental procedure is described as follows: during the melting process, the top and bottom halves of the furnace were set to $630 \text{ }^\circ\text{C}$ and $600 \text{ }^\circ\text{C}$ respectively while the liquidus temperature of the Al-35%Cu alloy was $554 \text{ }^\circ\text{C}$ as calculated by Thermo-Calc software [37]. As both halves reached their target temperatures, they were held at the temperatures for ~ 5 min to achieve a stable thermal gradient ($\sim 1 \text{ K}/\text{mm}$) in the melt. Following that, the solidification process was started by setting both the top and bottom furnace halves to a cooling rate of $\sim 2 \text{ K}/\text{min}$ with the temperature difference between two halves being kept unchanged. This positive thermal gradient was retained to ensure that the primary Al_2Cu intermetallic grew from bottom to top in order to facilitate the insertion of the sonotrode and hence the USMP application. To provide reference datasets, the growth of the primary Al_2Cu intermetallic was recorded *without* USMP application at

1 fps. In the case of experiments with USMP application, the sonotrode was inserted into the melt and USMP was applied when growing primary Al_2Cu intermetallic particles were observed in the camera field of view. The ultrasonic transducer power was 100 W for all the experiments. After ~ 5 s of USMP, the ultrasonic transducer was switched off and the sonotrode was lifted out of the melt. During the USMP application, the interaction of cavitation bubbles and acoustic streaming with the primary Al_2Cu intermetallic was recorded at 1000 fps. In addition, the subsequent solidification of the primary Al_2Cu intermetallic after USMP application was recorded at 4 fps. In total, 10 experiments were conducted with 5 reference experiments and 5 USMP experiments.

3. Experimental results

3.1. In-situ observation of primary Al_2Cu intermetallic growth without USMP

Fig. 2 shows a series of radiographs extracted from a video recording of the typical primary Al_2Cu intermetallic growth without USMP application. For brevity, only the most typical images were selected. A supplementary video (Video 001) is available in the online version of this publication. Primary Al_2Cu intermetallic dendrites mainly grew from the bottom right to the top left of the field of view with a thin, needle-like morphology. It is necessary to mention that this thin, needle-like morphology is actually a dendritic morphology with side arms, as will be clarified in the following sections. Note that it was impossible to determine where the primary Al_2Cu intermetallic dendrites nucleated and grew from based on the observation because the origin of dendrite growth was out of the radiography field of view, which could not cover the whole quartz tube crucible. However it is suggested that the dendrites could nucleate on impurities such as oxide particles present in the melt, or that the dendrites grew from crevices and/or defects of the quartz tube walls where capillary effect might play an important role. In fact, an interesting observation of intermetallic growth on oxide particles was recorded in some experiments and the results are now being processed by the authors and will be published elsewhere. Nevertheless, it is clear that, without the application of USMP, the primary Al_2Cu particles grew to a considerable length which extended beyond the whole recorded field of view, indicating that the length was greater than $2624 \mu\text{m}$ (the height of the field of view).

Supplementary video related to this article can be found at <http://dx.doi.org/10.1016/j.actamat.2017.09.010>.

3.2. Effect of USMP on the primary Al_2Cu intermetallic already grown into the field of view

Fig. 3(a) shows an image of primary Al_2Cu intermetallic particles that had already grown into the imaging field of view before USMP application. Again, they grew from bottom to top with a needle-like morphology to a length covering more than half of the field of view. Note that the growth inclination in Fig. 3 is from bottom left to top right which is different from the one in Fig. 2. This is probably due to the deviation in the thermal gradient caused by the side heat extraction from the small gap between the top and bottom furnaces. Ideally, the thermal gradient was supposed to be strictly vertically upwards, hence allowing primary Al_2Cu intermetallics to grow vertically upwards. However, in the real experiments, an aperture in the furnace was required for X-ray penetration and a small gap between the top and bottom furnace could not be eliminated. Therefore, side heat extraction from the thin channel through the gap was beyond our control. As a consequence, a change in the side heat extraction could affect the thermal gradient and hence the intermetallic growth direction. The frame of $t = -0.1$ s refers to 0.1 s before the USMP was started. As the USMP started and continued, the ultrasound-induced cavitation bubbles/clouds and acoustic streaming flow continuously fragmented the primary Al_2Cu particles and swept the fragments out of the field of view. Details can be found in the supplementary video (Video 002) in the online version. After 2.5 s of USMP application (the total USMP duration was ~ 5 s), all the primary Al_2Cu particles had been swept out of the field of view, as shown in Fig. 3(b). Different mechanisms of primary Al_2Cu intermetallic fragmentation and detachment were observed and will be described in the following sections.

Supplementary video related to this article can be found at <http://dx.doi.org/10.1016/j.actamat.2017.09.010>.

3.3. In-situ observation of primary Al_2Cu intermetallic fragmentation and detachment induced by a cavitation bubble cloud

A distinct primary Al_2Cu intermetallic fragmentation and detachment event observed during USMP was induced by a passing

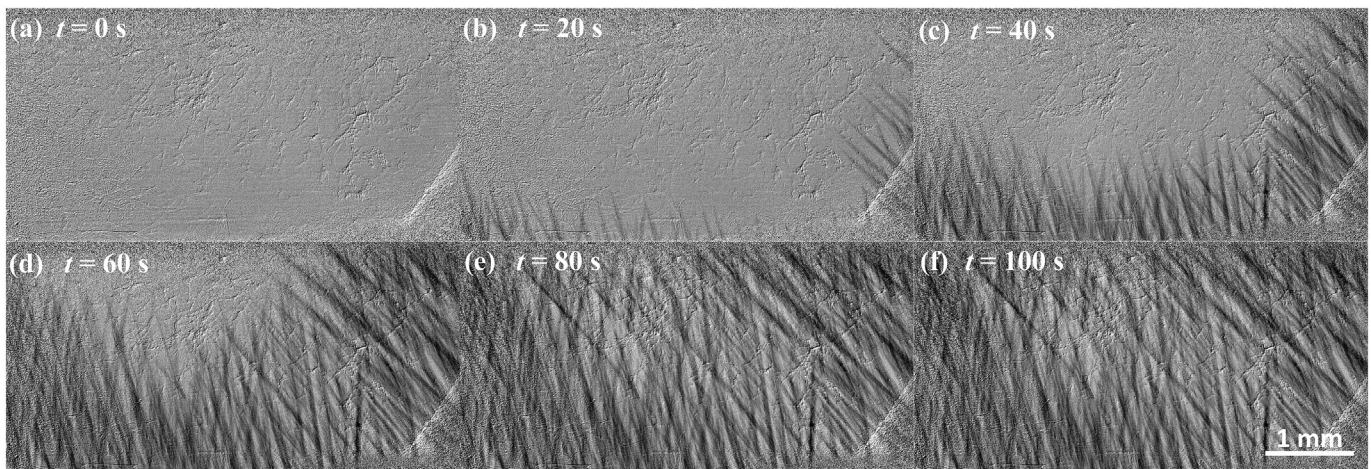


Fig. 2. Images of the primary Al_2Cu intermetallic growth without application of USMP. The field of view is $5120 \times 2624 \mu\text{m}^2$ and images were recorded at 1 fps. The $t = 0$ s frame was set as the frame before the appearance of primary Al_2Cu intermetallic in the field of view.

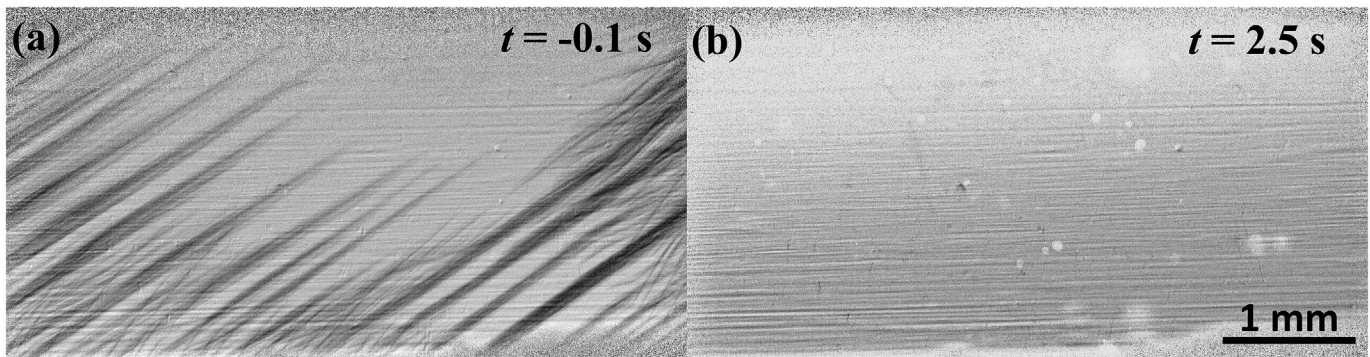


Fig. 3. Effect of USMP on the primary Al₂Cu intermetallic that was already grown in the field of view: (a) 0.1 s before USMP application and (b) after 2.5 s of USMP application. The field of view is 5120 × 2624 μm² and images were recorded at 1000 fps.

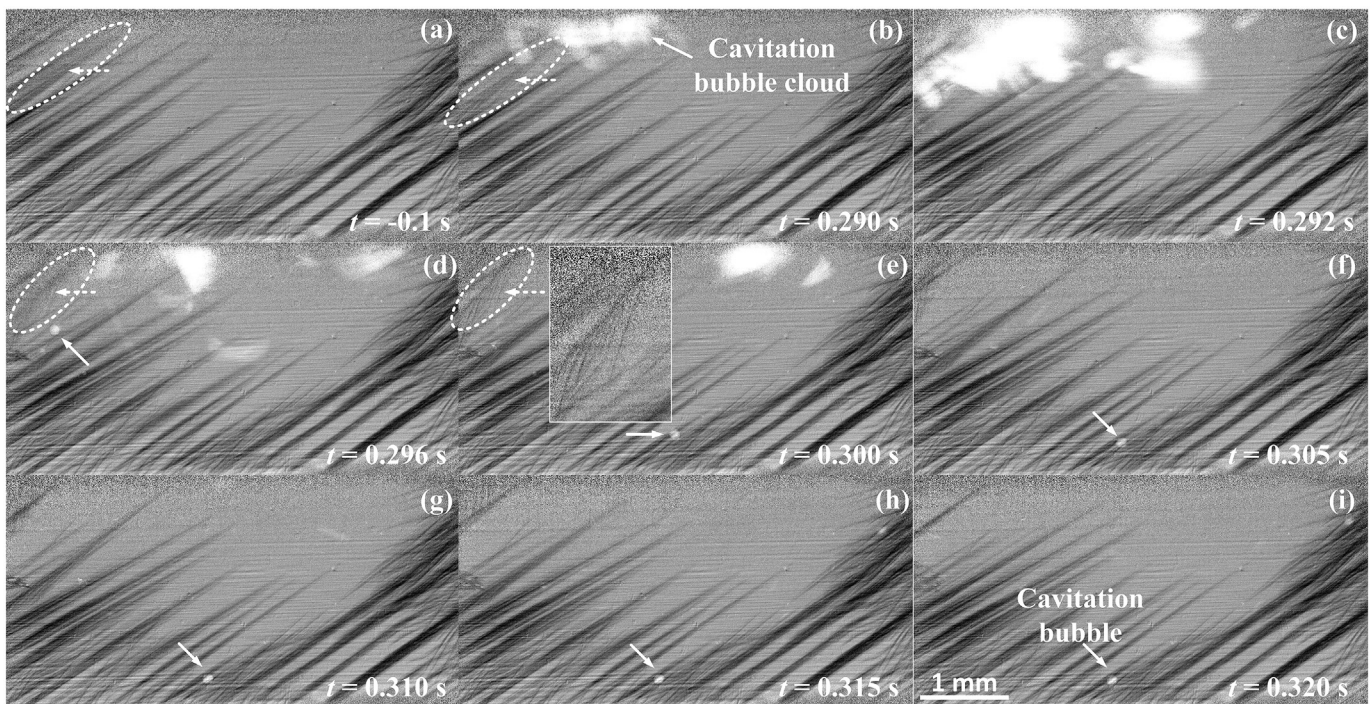


Fig. 4. Images of a passing cavitation bubble cloud breaking up the primary Al₂Cu intermetallic dendrites at the top corner of the field of view. The fragments were then swept out of the field of view by acoustic streaming flow. The inset in (e) is an enlarged image of the flipped dendrite indicated by the dash arrow. More details can be found in the supplementary video in the online version of this publication.

cavitation bubble cloud as shown in Fig. 4. The cavitation bubble cloud came into the field of view from the top left corner as shown in Fig. 4(b) and (c). The cloud then exited the field of view at the top right corner. The passage of this cavitation bubble cloud applied direct impact on the primary Al₂Cu intermetallics at the top left corner. One particular primary Al₂Cu dendrite is pointed out by the **dashed** arrow and is circled in Fig. 4(a) to (e). This intermetallic was fragmented and flipped by the impact created by the passing cavitation bubble cloud. The flipped fragment displayed clear dendrite morphology with side arms as shown in the inset of Fig. 4(e). This dendritic morphology can be frequently observed in the primary Al₂Cu fragments during USMP in the supplementary video (Video 003). After detachment, the fragment was swept out of the field of view by the acoustic streaming flow, as shown in Fig. 4(f) to (i). This observation of intermetallic fragmentation by a

passing cavitation bubble cloud is actually quite similar to the observation of intermetallic fragmentation reported in previous ultrasonic processing experiments with Al₃V intermetallic dendrites in water (Fig. 9 in Ref. [38]). However, a possibility that the fragmentation and removal of the Al₂Cu dendrite was simply caused by acoustic streaming flow which also transported the bubble cloud through the field of view cannot be ruled out. Note that an individual cavitation bubble became trapped between the dendrites as marked by the **solid** arrow in Fig. 4. It is suggested that the bubble became trapped as the main bubble cloud swept past the intermetallics, and could not escape due to the persistent acoustic streaming. It will be shown in Section 3.6 that this individual bubble later contributed to the intermetallic fragmentation.

Supplementary video related to this article can be found at <http://dx.doi.org/10.1016/j.actamat.2017.09.010>.

3.4. In-situ observation of primary Al_2Cu intermetallic fragmentation and detachment induced by acoustic streaming flow

The dominant primary Al_2Cu intermetallic fragmentation and detachment mechanism observed during USMP in the current experiment setup was caused by acoustic streaming flow. It was observed that the acoustic streaming flow not only caused remelting of primary Al_2Cu intermetallic dendrites at preferred positions, but also exerted force on the dendrites making them sway not unlike seagrass in an ocean current, eventually leading to detachment. Note that this fragmentation and detachment process was relatively long in duration (typically around 0.3 s) in comparison to other fragmentation processes (typically around 0.02 s). For brevity, only a few typical images, shown in Fig. 5, were selected to illustrate such a fragmentation and detachment event. A supplementary video (Video 004) is available in the online version of this

publication. The acoustic streaming flow pattern is indicated by the **dashed** arrow in Fig. 5(a). This acoustic streaming flow persisted for the entire duration of USMP, not only in this sequence but also in other sequences shown in the current paper. The streaming flow direction is not indicated in all of the images for reasons of clarity. Comparison of Fig. 5(a), (b) and (c) with special attention to the bottom left corner, shows progressive remelting of the intermetallic dendrites as highlighted in the dashed square. Careful examination of Fig. 5(d), (e) and (f) shows obvious deflection (swaying) of intermetallic dendrites marked as “A” and “B”. The double effect of continuing remelting and swaying caused by acoustic streaming flow finally led to the fragmentation and detachment as shown in Fig. 5(h), (i) and (j) for dendrite “B” and Fig. 5(m), (n) and (o) for dendrite “A”.

Supplementary video related to this article can be found at <http://dx.doi.org/10.1016/j.actamat.2017.09.010>.

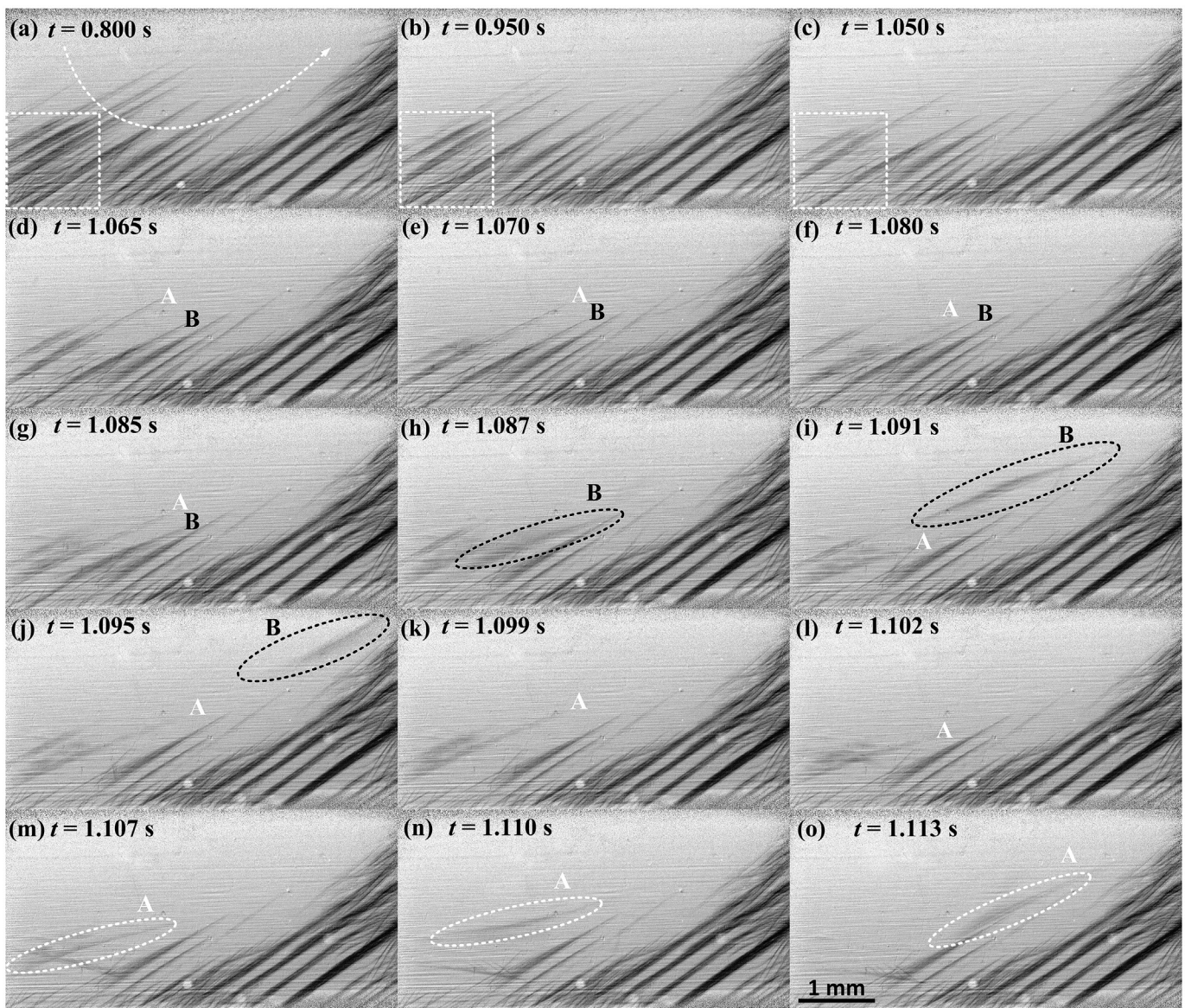


Fig. 5. Images of primary Al_2Cu intermetallic fragmentation and detachment caused by the combined effect of remelting and deflection induced by acoustic streaming flow. The bottom of the field of view is around 4.5 mm below the tip of sonotrode.

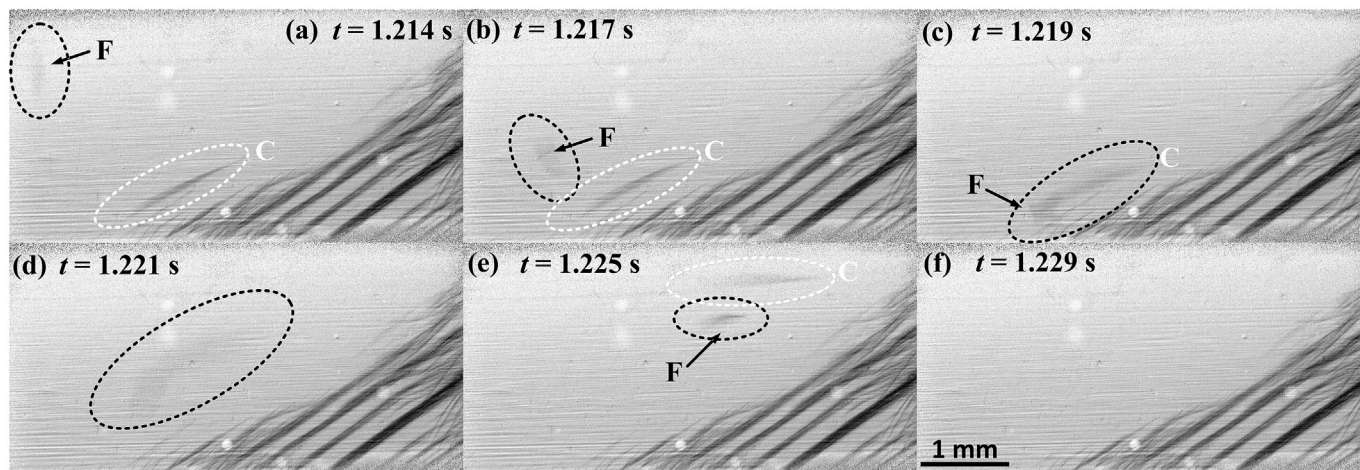


Fig. 6. Images showing a flowing fragment “F” colliding with a dendrite “C” and causing this dendrite “C” to fragment. The bottom of the field of view is around 4.5 mm below the tip of sonotrode.

3.5. In-situ observation of primary Al_2Cu intermetallic fragmentation and detachment induced by fragment collision

As the remelting and deflection effect caused by the acoustic streaming flow continued, a mechanism of fragmentation and detachment due to the collision of a flowing fragment with a partially-remelted dendrite was observed as exemplified in Fig. 6. It illustrates the collision of a fast-flowing fragment “F” with a partially-remelted dendrite “C”, breaking up the dendrite “C”, with the two fragments “F” and “C” then being transported out of the field of view. Although the dendrite “C” seemed already detached by the remelting and deflection effect, it was actually still connected to the solid bulk before the collision. This detail can be checked in the supplementary video (Video 005) in the online version of this publication. The speed of the flowing fragment “F” was estimated to be ~ 0.45 m/s.

Supplementary video related to this article can be found at <http://dx.doi.org/10.1016/j.actamat.2017.09.010>.

3.6. In-situ observation of primary Al_2Cu intermetallic fragmentation and detachment induced by a pulsating cavitation bubble

Another fragmentation mechanism of particular relevance to USMP was caused by a pulsating cavitation bubble. A typical example is illustrated by the selected images in Fig. 7. Although the bubble pulsation is not obvious in the still images in Fig. 7, clear bubble pulsation can be observed in the corresponding supplementary video (Video 006) in the online version of this publication. Examination of the selected images Fig. 7(a), (b) and (c) reveals that the dendrite in contact with the pulsating cavitation bubble experienced obvious bending, indicating that the pulsating cavitation bubble was applying force on this dendrite. The dendrite is marked as “D” in Fig. 7. Note that the pulsating cavitation bubble was originally captured between the dendrites during the passage of the cavitation bubble cloud, as previously discussed in Section 3.3 and shown in Fig. 4. Since dendrite “D” was also remelting due to the acoustic streaming flow, the impact produced by the pulsating cavitation bubble was finally sufficient to break up dendrite “D” as shown in Fig. 7(d) when the thickness of the primary dendrite apparently decreased to a critical value necessary for

fragmentation (see Section 4.1 for discussion). After detachment, fragment “D” was transported out of the field of view as shown in Fig. 7(e), (f) and (g). A similar fragmentation and detachment process also applied to another dendrite marked as “E” in Fig. 7(h) to (k). It is important to point out that the mechanism of fragmentation caused by oscillating deflection in the acoustic streaming flow as discussed above in Section 3.4 cannot be ruled out here.

Supplementary video related to this article can be found at <http://dx.doi.org/10.1016/j.actamat.2017.09.010>.

3.7. In-situ observation of primary Al_2Cu intermetallic growth after USMP application

Fig. 8 shows how the primary Al_2Cu intermetallic re-grew after USMP was terminated. The time $t = 0$ frame was defined as the frame when USMP ended and the sonotrode was lifted out of the melt. In Fig. 8(a), there was no obvious intermetallic growth in the field of view after 6 s. However, closer observation revealed small black features settling down in the melt in the field of view. These small features are considered to be the intermetallic fragments remaining after fragmentation and further melting in the hotter region and cavitation zone directly below the sonotrode. As cooling continued, the first intermetallic growth was observed at the bottom right corner as highlighted in Fig. 8(b). In addition, the dark features were observed to grow into small equiaxed intermetallic dendrites, as highlighted at the bottom left corner of the image. At this stage of solidification, it is thought that the intermetallics settled close to the bottom of the field of view, where the temperature was slightly lower as the thermal gradient was gradually establishing again after USMP. More equiaxed intermetallic dendrites growing from the small dark features were then observed in the field view, as highlighted in Fig. 8(c). This observation substantiates the fact that the small dark features were indeed intermetallic fragments that acted as nuclei for intermetallic growth. As solidification proceeded, the small equiaxed dendrites grew in size and settled on each other as shown in Fig. 8(d) to (g). Eventually the whole field of view was filled with equiaxed intermetallic dendrites that had grown from the small intermetallic fragments as shown in Fig. 8(h) and (i). The average size of the equiaxed dendrites was approximately $400 \mu\text{m}$, as estimated by measuring 60 equiaxed dendrites. This represents a remarkable refinement from the

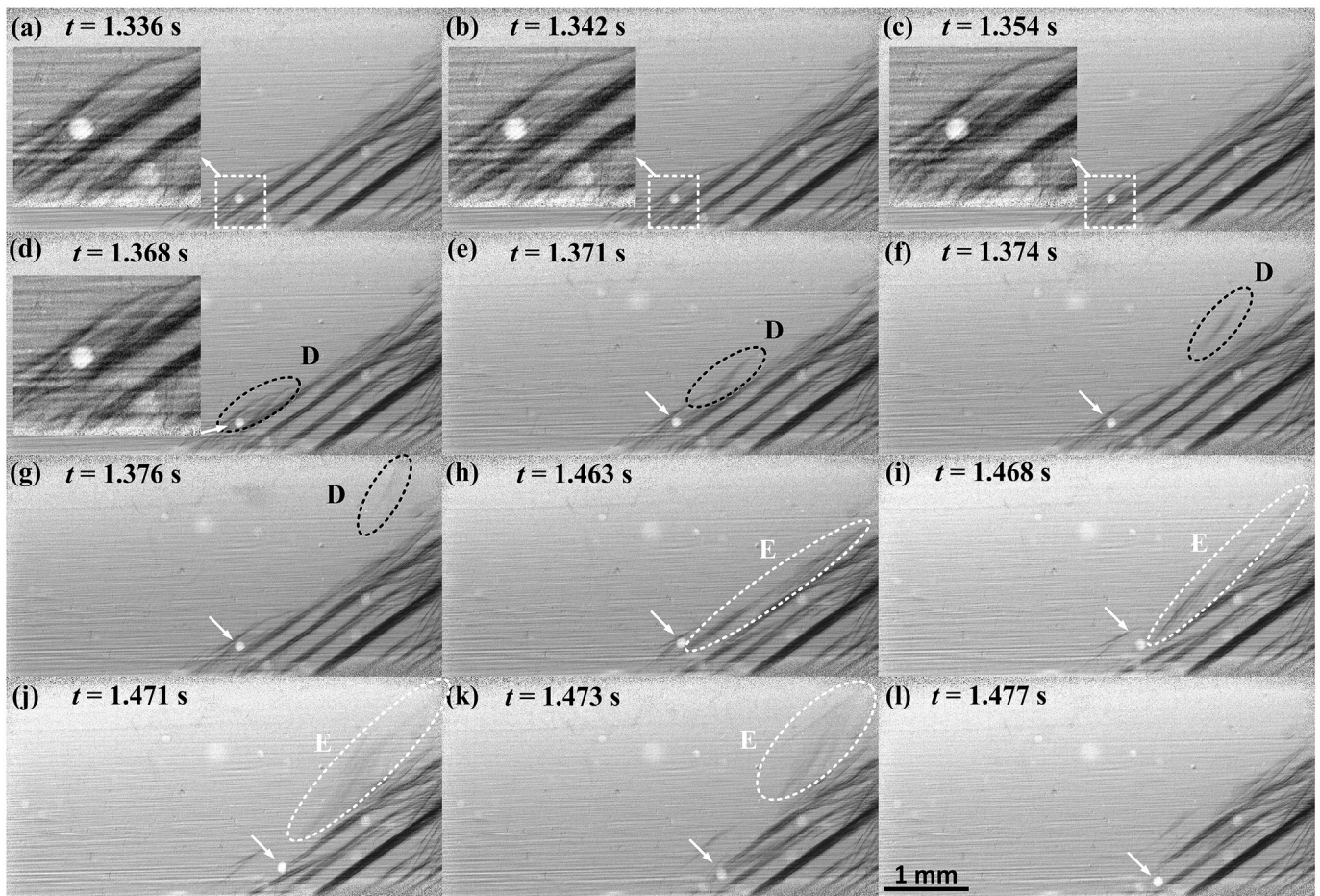


Fig. 7. Images showing a pulsating bubble breaking up two dendrites “D” and “E” that were partially remelted due to the acoustic streaming flow. The bottom of the field of view is around 4.5 mm below the tip of sonotrode.

approximately 2500 μm length of the original elongated dendrites for solidification without USMP. A particular intermetallic dendrite with continuous growth from a tiny fragment to an equiaxed dendrite is highlighted by the black dash square as enlarged in Fig. 8(j). More details can be found in the supplementary video (Video 007) in the online version of this paper.

Supplementary video related to this article can be found at <http://dx.doi.org/10.1016/j.actamat.2017.09.010>.

4. Discussion

4.1. Mechanisms of primary Al_2Cu intermetallic fragmentation during USMP

The fragmentation and detachment of crystals from a dendritic network has been a subject of study for decades in solidification science. The focus was mainly on the fragmentation of secondary dendrite arms under non-forced-convective conditions [24,25,27,39–46]. Previous in-situ experiments with transparent analogue alloys [42–45] and recent synchrotron radiography experiments with real metallic alloys [24,25,27] have clearly shown that the local solute enrichment due to tip velocity fluctuations or liquid flow, the local internal heat sources such as recalescence from eutectic solidification and the natural coarsening/ripening, are potent mechanisms for initiation of local remelting and hence fragmentation of secondary dendrite arms. It is further demonstrated that dendrite root remelting induced by solute pileup is the

primary fragmentation mechanism under non-convective conditions. In addition, the bending stress due to dynamic pressure of natural thermosolutal convective flow against dendrite was once considered as a potential mechanism for fragmentation [47]. However, rough estimates [47] based on bending moments and fluid-flow calculations indicate that mechanical breakdown of a dendrite is unlikely under non-forced convective conditions in normal castings.

Recently, a number of studies have been conducted on dendrite fragmentation under the presence of enhanced convective flow induced by external fields such as electromagnetic and ultrasound fields [17,18,38,48–50]. The observation of dendrite fragmentation induced by electromagnetic stirring [48–50] showed that the root remelting driven by solute accumulation due to transportation of solute-rich liquid via enhanced convective flow, still acts as the principal mechanism for the fragmentation in the presence of an electromagnetic field. In contrast, studies [18,36,38] on the fragmentation caused by USMP revealed that the pressure created during the implosion of cavitation bubbles or bubble clouds and produced by pulsating cavitation bubbles imparted sufficient force to directly fracture a solid particle or to cause a pre-existing crack in a solid particle to propagate to the critical length at which point fracture occurs. The acoustic streaming flow was considered to have less effect on fragmentation, instead only transferring the fragments throughout the melt [18,38].

However, under the current experimental conditions, chosen region of observation and for the elongated morphology of

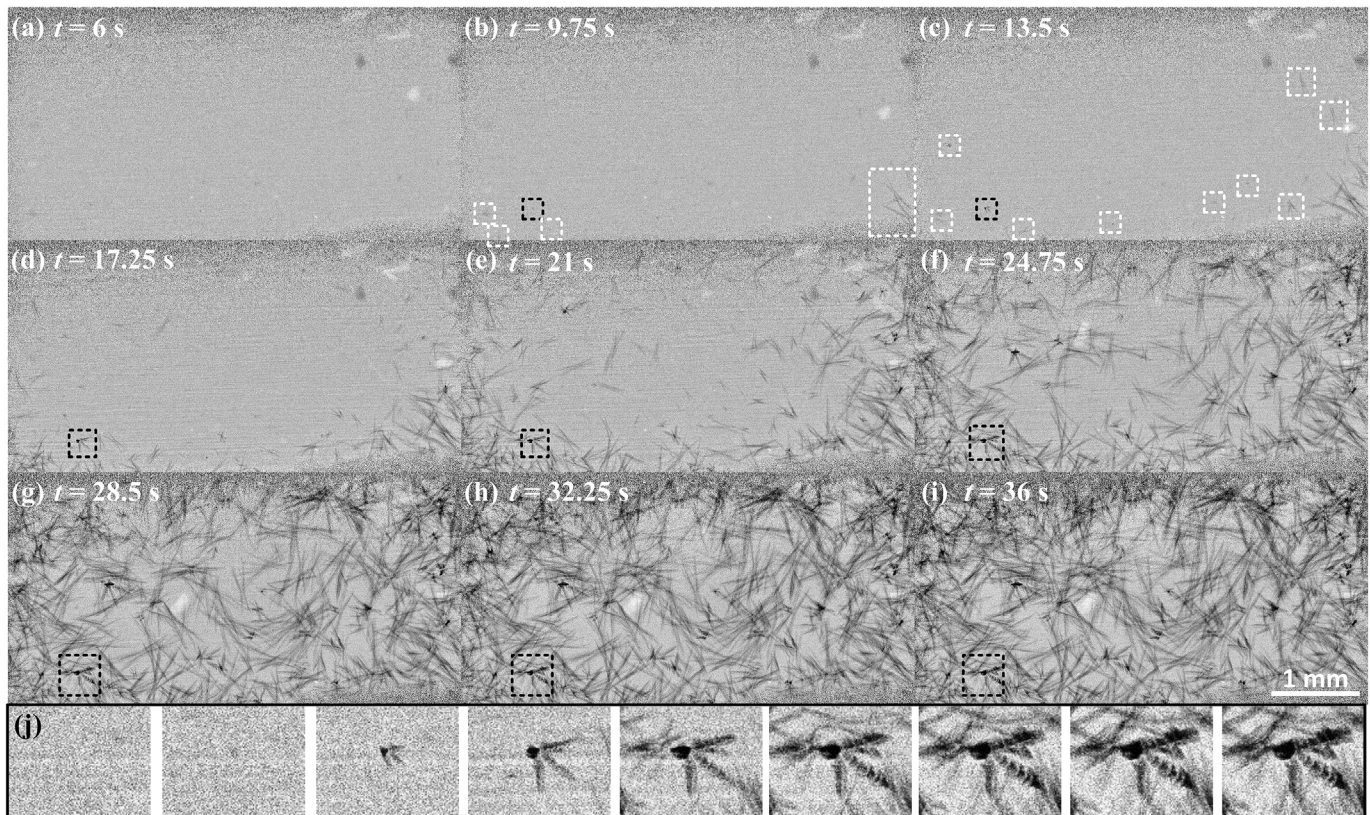


Fig. 8. Images showing intermetallic fragments growing into equiaxed intermetallic dendrites filling the whole field of view after USMP stopped. The field of view is $5120 \times 2624 \mu\text{m}^2$ and images were recorded at 4 fps. The $t = 0$ s frame was defined as the frame when the USMP was switched off and the sonotrode was lifted out of the melt. (j) The sequence of the enlarged images as highlighted by the black dashed square. The bottom of the field of view is around 4.5 mm below the tip of sonotrode.

intermetallic dendrites, it appears that the remelting and deflection caused by acoustic streaming flow was the dominant fragmentation mechanism during USMP. It is well demonstrated that the acoustic streaming flow induced by the ultrasonic source in a finite volume circulates in the whole volume with attenuation and is considered as macroscopic flow [1,3]. In the present experimental setup with the sonotrode positioned at the top of the sample tube, the acoustic streaming flow would transport liquid down from the upper part of the sample tube to the imaging field of view 2 mm below the sonotrode tip. At the top of the sample tube, the melt temperature was higher (positive thermal gradient) and the melt had a nominal composition of 35% Cu. Recall that 35% Cu is a hypereutectic composition and therefore the transport of Cu-rich liquid from the upper part of the liquid volume would actually promote primary Al_2Cu intermetallic growth in the field of view where the liquid phase contained less than 35% Cu according to the Al-Cu equilibrium phase diagram. As a consequence, the underlying cause of remelting could only arise from the continuous transportation of hotter liquid into the solidification zone observed in the X-ray images.

Then there is the swaying deflection effect caused by acoustic streaming flow, from which we infer there is a force applied to the dendrites. The deflection prevailed in the fragmentation process observed here, probably due to two significant differences between our present work and previous studies: (1) the larger velocity of the acoustic streaming flow and (2) the elongated shape of the primary Al_2Cu intermetallic dendrites which grew prior to the application of USMP. The velocity of the acoustic streaming flow was approximately 0.5 m/s, as calculated by measuring the displacement of the same fragments over several frames. This value agrees well with

acoustic stream flow velocities reported in the literature [3] and is much larger than the velocity values (order of 0.01 m/s) used for the analysis in previous work [47]. In addition, the deflection due to acoustic streaming was applied directly to long primary dendrites, so that they appear to sway elastically. For example, the lengths of dendrite “A” and “B” in Fig. 5 are $2340 \mu\text{m}$ and $2600 \mu\text{m}$ respectively. To assess the mechanical stress on the primary dendrites associated with the acoustic streaming flow, the simple model developed by Pilling and Hellawell [47] was adopted to analyse the behaviour of dendrites “A” and “B” in Fig. 5. A schematic of the Pilling-Hellawell model is shown in Fig. 9(a) and the details are described as follows:

$$\sigma = \frac{-M \cdot r}{I(r)} \quad (1)$$

$$M = \frac{-FL^2}{2} \quad (2)$$

$$F = 3 \cdot \pi \cdot \eta \cdot V \quad (3)$$

$$I(r) = \frac{\pi \cdot r^4}{4} \quad (4)$$

Here M is the bending moment, I is the moment of inertia of the section, and r is the radius, F is the force per unit length acting on the dendrite, L is the length, η is the dynamic viscosity, and V is the flow velocity.

The lengths with force application, L_A and L_B , are assumed as the lengths of the detached fragments which are roughly $2000 \mu\text{m}$ and

2200 μm respectively. The radius, r , is assumed to decrease from 100 μm to 5 μm considering that the dendrites were thinning due to remelting. Note that this large range was selected to ensure all possibilities. In fact the maximum radius of dendrites measured in Fig. 5 was around 60 μm and the minimum radius was about 5 μm as estimated from the width of the flowing fragments. The viscosity of an Al-35% Cu melt, η , was taken as $2.2 \times 10^{-3} \text{ kg m}^{-1} \text{ s}^{-1}$, which was the viscosity for the Al-33% Cu at 550 $^{\circ}\text{C}$ available from Ref. [51]. Based on the above assumptions, the variation of flow-induced stress with decreasing radius is calculated as shown in Fig. 9(b). The yield strength of Al_2Cu intermetallic at 550 $^{\circ}\text{C}$ is estimated by the method of Frost and Ashby [52] to be approximately 20 MPa. The details are described in the Appendix. As we can see, when the radius decreases to 11 μm , the stresses on dendrite “A” and “B” reaches 20 MPa and 24 MPa respectively, indicating that the mechanical breakdown of the primary Al_2Cu intermetallic dendrite by the stress induced by acoustic streaming flow is possible, considering the concurrent remelting.

The cavitation bubbles and bubble clouds also contribute to fragmentation, not only by mechanically breaking up the dendrites but also by facilitating the effect of acoustic streaming flow on dendrites. The observed fragmentation events induced by individual cavitation bubbles or bubble clouds are consistent with those observed in the previous studies by the authors [38] and by Shu et al. [18] for primary intermetallics in water and for a transparent analogue, respectively. This further confirms that the pressure created by bubble pulsation and implosion is sufficient to induce fragmentation either via progressive crack propagation to a critical length or via instant mechanical fracture. Importantly, the initial fragmentation and detachment induced by cavitation bubble clouds opens up the dendrite network, allowing acoustic streaming flow to come into contact with the primary dendrites, assisting the acoustic streaming flow in fragmentation. In addition, the collision of flowing fragments with the remelting dendrites also contributed to the fragmentation rate.

It is important to point out that the experiments presented here involved a few unique features that may not be typical of USMP of bulk melts. These features were necessary to enable synchrotron X-ray high speed radiography observation of USMP. The first one is the imposed thermal gradient ($\sim 1 \text{ K/mm}$) which forced the intermetallic to grow from the bottom to the top in order to facilitate the observation of USMP effects. Under the imposed thermal gradient, the primary Al_2Cu intermetallic dendrites grew to long needle morphology. The second one is the relatively thin thickness of the channel where the alloy was contained and all the observations were made. As mentioned in the experimental section, the thin channel was designed for easy X-ray penetration for high speed radiography. Although extra care was taken to make sure that the sonotrode ($\varnothing = 1 \text{ mm}$) was placed strictly vertical towards the gap

between the walls of the thin channel ($\sim 300 \mu\text{m}$) to minimize the reflection from the channel walls, minor reflections of sound waves would still be expected. Nevertheless, the observed flow patterns indicated by the flowing fragments in the field of view as shown in supplementary videos 002, 003, 004, 005, 006, show that the acoustic flow went always anti-clockwise and no evident change of the flow direction could be observed, which implies that the reflection from the channel wall was negligible. Furthermore, as mentioned above, the magnitude of the measured flow velocity in the present experiment is in the same order of magnitude as those reported in the literature, also implying a minor reflection enhancing effect.

It is also necessary to mention that the acoustic streaming flow may facilitate temperature uniformity in the treated volume. As a result, the effect of thermal remelting reported here may be less pronounced than in the present experiments where a well-established thermal gradient was present. In addition, in the case where the primary phase is ductile and grows to well-developed, coarse, equiaxed, freely-flowing dendrites, the strong role of acoustic streaming flow in fragmenting the intermetallic dendrites may not be the dominant mechanism.

4.2. Mechanisms of primary Al_2Cu intermetallic refinement induced by USMP

A straightforward comparison between Figs. 2 and 8(i) confirms significant primary Al_2Cu intermetallic refinement induced by USMP via fragmentation. The image sequences shown in Figs. 3–8 (also with the corresponding videos) undoubtedly demonstrated that applying USMP during the growth stage of intermetallic dendrites results in the effective fragmentation of intermetallic dendrites via acoustic cavitation bubble pulsation or/and implosion and acoustic streaming flow.

Although we could not observe the further travel path of the detached dendrite fragments (due to the size and position of the imaging field of view), we know from the flow pattern that they were transported upward toward the cavitation zone below the sonotrode. After the end of USMP, small nuclei representing the surviving fragments showered downward into the field of view. The mechanism of microstructural refinement due to USMP is described as follows:

As the acoustic flow continuously circulates the detached fragments throughout the melt, the ongoing fragmentation produces a large number of small fragments. Many of these small fragments survive and act as nuclei for the intermetallic dendrites during subsequent solidification, finally leading to refinement. A schematic to illustrate the refinement mechanism is shown in Fig. 10.

Note that, when USMP is applied prior to the occurrence of any clear nucleation events or in the early stage of nucleation, the

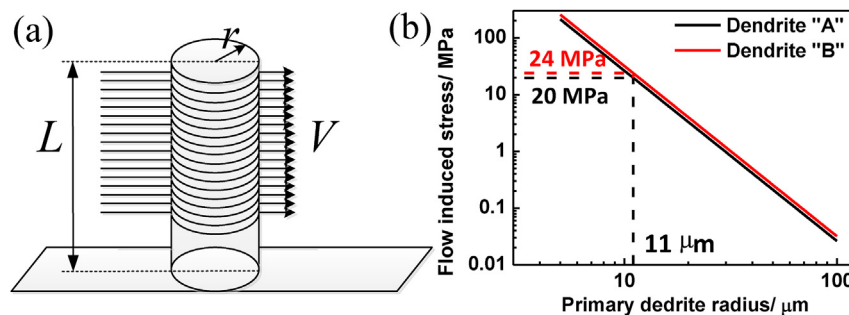


Fig. 9. (a) A schematic showing the stress associated with the acoustic streaming flow against the primary dendrite; (b) the variation of stress induced by acoustic streaming flow on the primary dendrite with the decreasing dendrite radius.

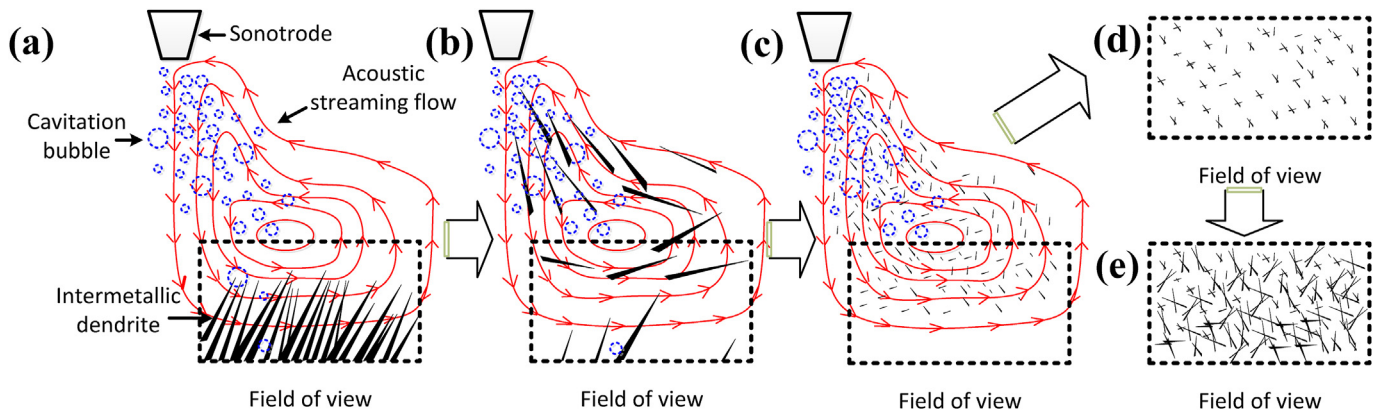


Fig. 10. A schematic illustrating the mechanism for microstructural refinement of primary intermetallic dendrites induced by USP: (a) USP application generates acoustic cavitation and acoustic streaming flow; (b) intermetallic dendrites are fragmented due to the combined effects of the acoustic cavitation and streaming flow; (c) further fragmentation as the acoustic flow continuously circulates the fragments back into the cavitation zone resulting in large number of small fragments; (d) after USP is stopped, the surviving small fragments sink downwards and grow as equiaxed dendrites; (e) as the equiaxed dendrites grow further, they impinge on each other, leading to refinement.

dominant refinement mechanism is essentially the cavitation-enhanced heterogeneous nucleation as mentioned in the Introduction, while this paper is focused on the refinement effect as a consequence of the cavitation-induced fragmentation.

5. Conclusions

The effect of USMP on the pre-existing primary Al_2Cu intermetallics in an Al-35% Cu alloy during solidification was studied using high speed synchrotron X-ray radiography. The dynamic fragmentation processes of well-grown Al_2Cu intermetallic dendrites induced by USMP and the subsequent solidification of the alloy which was contained in a thin channel of $\sim 300 \mu\text{m}$ thickness were recorded at high frame rates (1000 fps) for the first time.

In-situ observations clearly demonstrated that USMP induced fragmentation of primary intermetallic dendrites via acoustic cavitation and acoustic streaming flow, through various mechanisms. The remelting due to transport of hot liquid to the intermetallic dendrites via acoustic streaming flow and the stress associated with the acoustic streaming flow acting on the elongated intermetallic dendrites are suggested as the dominant fragmentation mechanisms in the present experiments. In addition, cavitation bubbles or bubble clouds also play an important role in fragmentation because they not only mechanically break up the intermetallic dendrites by the pressure generated during pulsation and/or implosion but also facilitate the effects of acoustic streaming flow by opening up the intermetallic dendrite network.

Clear observation of equiaxed intermetallic dendrites growing from small fragments and eventually leading to intermetallic refinement provides the first conclusive evidence for the cavitation-induced fragmentation theory that was proposed for USMP-induced refinement. The acoustic cavitation and acoustic streaming flow induced by USMP progressively break up the intermetallic dendrites into small fragments and many of these small fragments survive and then act as nuclei for the intermetallic in the subsequent solidification, leading to the growth of equiaxed intermetallic dendrites and hence intermetallic refinement. Similar mechanisms may be applicable to refinement of other primary phases in other alloy systems.

Acknowledgements

The authors acknowledge financial support from the UK Engineering and Physical Science Research Council (EPSRC) for the

Ultra-Cast project (grants EP/L019884/1; EP/L019825/1; EP/L019965/1). Mi also would like to acknowledge the financial support by the Royal Society Industry Fellowship awarded in 2012–2016. The experiments were performed on the Psiché beamline at Synchrotron SOLEIL, France (Proposal No. 2016076). Beamline I12 at Diamond Light Source, UK, is also thanked for loan of the high speed camera.

Appendix

The method proposed by Frost and Ashby [52] for calculating the yield strength at temperature close to the melting temperature:

$$\sigma_y = 10^{-3} \cdot E(T)$$

$$E(T) = E_{300} \left(1 + B \cdot \left(\frac{T - 300}{T_m} \right) \right)$$

where σ_y is the yield strength; $E(T)$ is the Young's modulus at an absolute temperature T ; E_{300} is the modulus at 300 K and T_m is the absolute melting temperature. The incipient melting temperature of Al_2Cu intermetallic is around 864 K [53] and the melt temperature is estimated to be approximately 823 K (550 °C). The E_{300} of Al_2Cu intermetallic is measured as 104 GPa [54] while the constant B is taken as -1.33 [47]. Inputting all the above values, it is estimated that the yield strength of Al_2Cu intermetallic at 550 °C is ~ 20 MPa.

References

- [1] O.V. Abramov, *High-intensity Ultrasonics: Theory and Industrial Applications*, Gordon and Breach Science Publishers, Amsterdam, The Netherlands, 1998.
- [2] G.I. Eskin, Broad prospects for commercial application of the ultrasonic (cavitation) melt treatment of light alloys, *Ultrason. Sonochem* 8 (2001) 319–325.
- [3] G.I. Eskin, D.G. Eskin, *Ultrasonic Treatment of Light Alloy Melts*, second ed., CRC Press, Boca Raton, Florida, 2015.
- [4] J.R.G. Sander, B.W. Zeiger, K.S. Suslick, Sonocrystallization and sono-fragmentation, *Ultrason. Sonochem* 21 (2014) 1908–1915.
- [5] T.V. Atamanenko, D.G. Eskin, L. Zhang, L. Katgerman, Criteria of grain refinement induced by ultrasonic melt treatment of aluminum alloys containing Zr and Ti, *Metall. Mater. Trans. A* 41 (2010) 2056–2066.
- [6] M. Qian, A. Ramirez, A. Das, Ultrasonic refinement of magnesium by cavitation: clarifying the role of wall crystals, *J. Cryst. Growth* 311 (2009) 3708–3715.
- [7] J.D. Hunt, K.A. Jackson, Nucleation of solid in an undercooled liquid by cavitation, *J. Appl. Phys.* 37 (1966) 254–257.
- [8] J.J. Frawley, W.J. Childs, Grain refinement by ultrasonic vibrations of bismuth,

- tin, and bismuth-tin alloys, *Met Soc AIME-Trans.* 245 (1969) 2399–2404.
- [9] F. Wang, D. Eskin, J. Mi, T. Connolly, J. Lindsay, M. Mounib, A refining mechanism of primary Al_3Ti intermetallic particles by ultrasonic treatment in the liquid state, *Acta Mater.* 116 (2016) 354–363.
- [10] H.N. Kim, K.S. Suslick, Sonofragmentation of ionic crystals, *Chem. – A Eur. J.* 23 (2017) 2778–2782.
- [11] G.I. Eskin, D.G. Eskin, Some control mechanisms of spatial solidification in light alloys, *Z. Met.* 95 (2004) 682–690.
- [12] T.V. Atamanenko, D.G. Eskin, M. Sluiter, L. Katgerman, On the mechanism of grain refinement in Al–Zr–Ti alloys, *J. Alloys Compd.* 509 (2011) 57–60.
- [13] L. Zhang, D.G. Eskin, A.G. Miroux, L. Katgerman, On the mechanism of the formation of primary intermetallics under ultrasonic melt treatment in an Al–Zr–Ti alloy, *IOP Conf. Ser. Mater. Sci. Eng.* 27 (2012), 012002.
- [14] G.M. Swallowe, J.E. Field, C.S. Rees, A. Duckworth, A photographic study of the effect of ultrasound on solidification, *Acta Metall.* 37 (1989) 961–967.
- [15] R. Chow, R. Blindt, R. Chivers, M. Povey, The sonocrystallisation of ice in sucrose solutions: primary and secondary nucleation, *Ultrasonics* 41 (2003) 595–604.
- [16] Z. Guo, A.G. Jones, N. Li, S. Germana, High-speed observation of the effects of ultrasound on liquid mixing and agglomerated crystal breakage processes, *Powder Technol.* 171 (2007) 146–153.
- [17] R.M. Wagterveld, L. Boels, M.J. Mayer, G.J. Witkamp, Visualization of acoustic cavitation effects on suspended calcite crystals, *Ultrason. Sonochem.* 18 (2011) 216–225.
- [18] D. Shu, B. Sun, J. Mi, P.S. Grant, A high-speed imaging and modeling study of dendrite fragmentation caused by ultrasonic cavitation, *Metall. Mater. Trans. A* 43 (2012) 3755–3766.
- [19] J. Wang, P.D. Lee, R.W. Hamilton, M. Li, J. Allison, The kinetics of Fe-rich intermetallic formation in aluminium alloys: in situ observation, *Scr. Mater.* 60 (2009) 516–519.
- [20] A. Bogno, H. Nguyen-Thi, A. Buffet, G. Reinhart, B. Billia, N. Mangelinck-Noël, N. Bergeon, J. Baruchel, T. Schenk, Analysis by synchrotron X-ray radiography of convection effects on the dynamic evolution of the solid–liquid interface and on solute distribution during the initial transient of solidification, *Acta Mater.* 59 (2011) 4356–4365.
- [21] H. Yasuda, I. Ohnaka, K. Kawasaki, A. Sugiyama, T. Ohmichi, J. Iwane, K. Umetani, Direct observation of stray crystal formation in unidirectional solidification of Sn–Bi alloy by X-ray imaging, *J. Cryst. Growth* 262 (2004) 645–652.
- [22] B. Li, H.D. Brody, A. Kazimirov, Real-time observation of dendrite coarsening in Sn–13%Bi alloy by synchrotron microradiography, *Phys. Rev. E* 70 (2004), 062602.
- [23] P.D. Lee, J.D. Hunt, Hydrogen porosity in directional solidified aluminium–copper alloys: in situ observation, *Acta Mater.* 45 (1997) 4155–4169.
- [24] R.H. Mathiesen, L. Arnberg, X-ray radiography observations of columnar dendritic growth and constitutional undercooling in an Al–30wt%Cu alloy, *Acta Mater.* 53 (2005) 947–956.
- [25] R.H. Mathiesen, L. Arnberg, P. Bleuet, A. Somogyi, Crystal fragmentation and columnar-to-equiaxed transitions in Al–Cu studied by synchrotron X-ray video microscopy, *Metall. Mater. Trans. A* 37 (2006) 2515–2524.
- [26] H. Nguyen-Thi, G. Reinhart, N. Mangelinck-Noël, H. Jung, B. Billia, T. Schenk, J. Gastaldi, J. Härtwig, J. Baruchel, In-situ and real-time investigation of columnar-to-equiaxed transition in metallic alloy, *Metall. Mater. Trans. A* 38 (2007) 1458–1464.
- [27] D. Ruvalcaba, R.H. Mathiesen, D.G. Eskin, L. Arnberg, L. Katgerman, In situ observations of dendritic fragmentation due to local solute-enrichment during directional solidification of an aluminum alloy, *Acta Mater.* 55 (2007) 4287–4292.
- [28] T.L. Lee, J.C. Khong, K. Fezzaa, J. Mi, Ultrafast X-ray imaging and modelling of ultrasonic cavitations in liquid metal, *Mater. Sci. Forum* 765 (2013) 190–194.
- [29] D. Tan, T.L. Lee, J.C. Khong, T. Connolly, K. Fezzaa, J. Mi, High-speed synchrotron x-ray imaging studies of the ultrasound shockwave and enhanced flow during metal solidification processes, *Metall. Mater. Trans. A* 46 (2015) 2851–2861.
- [30] J. Mi, D. Tan, T.L. Lee, In situ synchrotron x-ray study of ultrasound cavitation and its effect on solidification microstructures, *Metall. Mater. Trans. B* 46 (2015) 1615–1619.
- [31] I. Tzanakis, W.W. Xu, D.G. Eskin, P.D. Lee, N. Kotsovinos, In situ observation and analysis of ultrasonic capillary effect in molten aluminium, *Ultrason. Sonochem.* 27 (2015) 72–80.
- [32] H. Huang, D. Shu, Y. Fu, J. Wang, B. Sun, Synchrotron radiation X-ray imaging of cavitation bubbles in Al–Cu alloy melt, *Ultrason. Sonochem.* 21 (2014) 1275–1278.
- [33] W.W. Xu, I. Tzanakis, P. Srirangam, W.U. Mirihanage, D.G. Eskin, A.J. Bodey, P.D. Lee, Synchrotron quantification of ultrasound cavitation and bubble dynamics in Al–10Cu melts, *Ultrason. Sonochem.* 31 (2016) 355–361.
- [34] W. Mirihanage, W. Xu, J. Tamayo-Arztondo, D. Eskin, M. Garcia-Fernandez, P. Srirangam, P. Lee, Synchrotron radiographic studies of ultrasonic melt processing of metal matrix nano composites, *Mater. Lett.* 164 (2016) 484–487.
- [35] A. King, N. Guignot, P. Zerbino, E. Boulard, K. Desjardins, M. Bordessoule, N. Leclercq, S. Le, G. Renaud, M. Cerato, M. Bornert, N. Lenoir, S. Delzon, J.-P. Perrillat, Y. Legodec, J.-P. Itié, Tomography and imaging at the PSICHE beam line of the SOLEIL synchrotron, *Rev. Sci. Instrum.* 87 (2016), 093704.
- [36] B. Wang, D. Tan, T.L. Lee, J.C. Khong, F. Wang, D. Eskin, T. Connolly, K. Fezzaa, J. Mi, Ultrafast synchrotron X-ray imaging studies of the mechanisms of microstructure fragmentations in solidification under ultrasound, *Acta Mater.* (submitted for publication).
- [37] J.O. Andersson, T. Helander, L. Höglund, P. Shi, B. Sundman, Thermo-Calc & DICTRA, computational tools for materials science, *Calphad* 26 (2002) 273–312.
- [38] F. Wang, I. Tzanakis, D. Eskin, J. Mi, T. Connolly, In situ observation of ultrasonic cavitation-induced fragmentation of the primary crystals formed in Al alloys, *Ultrason. Sonochem.* 39 (2017) 66–76.
- [39] K. Jackson, J. Hunt, D. Uhlmann, T. Seward, On origin of equiaxed zone in castings, *Trans. Metall. Soc. AIME* 236 (1966) 149.
- [40] S.M. Copley, A.F. Giamei, S.M. Johnson, M.F. Hornbecker, The origin of freckles in unidirectionally solidified castings, *Metall. Trans.* 1 (1970) 2193–2204.
- [41] R. Mehrabian, M.A. Keane, M.C. Flemings, Experiments on macrosegregation and freckle formation, *Metall. Trans.* 1 (1970) 3238–3241.
- [42] T. Sato, W. Kurz, K. Ikawa, Experiments on dendrite branch detachment in the succinonitrile–camphor alloy, *Trans. Jpn. Inst. Metals* 28 (1987) 1012–1021.
- [43] A. Hellawell, S. Liu, S.Z. Lu, Dendrite fragmentation and the effects of fluid flow in castings, *JOM* 49 (1997) 18–20.
- [44] C.J. Paradies, R.N. Smith, M.E. Glicksman, The influence of convection during solidification on fragmentation of the mushy zone of a model alloy, *Metall. Mater. Trans. A* 28 (1997) 875–883.
- [45] S. Liu, S.-Z. Lu, A. Hellawell, Dendritic array growth in the systems NH_4Cl-H_2O and $[CH_2CN]_2-H_2O$: the detachment of dendrite side arms induced by deceleration, *J. Cryst. Growth* 234 (2002) 740–750.
- [46] G. Hansen, A. Hellawell, S.Z. Lu, R.S. Steube, Some consequences of thermo-solutal convection: the grain structure of castings, *Metall. Mater. Trans. A* 27 (1996) 569–581.
- [47] J. Pilling, A. Hellawell, Mechanical deformation of dendrites by fluid flow, *Metall. Mater. Trans. A* 27 (1996) 229–232.
- [48] E. Liotti, A. Lui, R. Vincent, S. Kumar, Z. Guo, T. Connolly, I.P. Dolbnya, M. Hart, L. Arnberg, R.H. Mathiesen, P.S. Grant, A synchrotron X-ray radiography study of dendrite fragmentation induced by a pulsed electromagnetic field in an Al–15Cu alloy, *Acta Mater.* 70 (2014) 228–239.
- [49] E. Liotti, A. Lui, S. Kumar, Z. Guo, C. Bi, T. Connolly, P.S. Grant, The spatial and temporal distribution of dendrite fragmentation in solidifying Al–Cu alloys under different conditions, *Acta Mater.* 121 (2016) 384–395.
- [50] T. Campanella, C. Charbon, M. Rappaz, Grain refinement induced by electromagnetic stirring: a dendrite fragmentation criterion, *Metall. Mater. Trans. A* 35 (2004) 3201–3210.
- [51] S. Ganesan, R. Speiser, D.R. Poirier, Viscosities of aluminum-rich Al–Cu liquid alloys, *Metall. Trans. B* 18 (1987) 421–424.
- [52] H.J. Frost, M.F. Ashby, *Deformation Mechanism maps: The Plasticity and Creep of Metals and Ceramics*, Pergamon Press, 1982.
- [53] T.B. Massalski, The Al–Cu (Aluminum–Copper) system, *Bull. Alloy Phase Diagrams* 1 (1980) 27–33.
- [54] J. Westbrook, R. Fleischer, *Intermetallic compounds, Vol. 2, Basic Mechanical Properties and Lattice Defects of Intermetallic Compounds*, Wiley.